2024

Finite element modelling of fully encapsulated cable bolts in laboratory large scale pull out test

Ashkan Rastegarmanesh

Ali Mirzaghorbanali

Kevin McDougall

Naj Aziz

Sina Anzanpour

See next page for additional authors

Authors

Ashkan Rastegarmanesh, Ali Mirzaghorbanali, Kevin McDougall, Naj Aziz, Sina Anzanpour, and Hadi Nourizadeh

FINITE ELEMENT MODELLING OF FULLY ENCAPSULATED CABLE BOLTS IN LABORATORY LARGE SCALE PULL OUT TEST

Ashkan Rastegarmanesh[1], Ali Mirzaghorbanali[2], Kevin McDougall[3], Naj Aziz[4], Sina Anzanpour[5], Hadi Nourizadeh[6]

ABSTRACT: Modelling cable bolts in numerical software is a challenging task. Cables are made from multiple strands wound together and when loaded, they tend to act in a way more complex manner than rock bolts. This study used laboratory data from large scale pull out testing of fully encapsulated cable bolts using cementitious grout. A finite element method was adopted and a series of engineering simplifications and assumptions were made to increase the efficiency of the model. The results were able to illustrate a better capability in modelling the bulbed cables compared to the plain cables. Also, the sensitivity analysis proposed that increasing cable diameter for a given hole size (decreasing grout annulus thickness) can increase the overall peak load value, similar to an increase in concrete confinement, grout uniaxial compressive strength, and bulb size.

INTRODUCTION

Modelling rock bolts and cable bolts in numerical software is not a new undertaking. Various studies have been carried out; however, most studies are focused on rock bolts. Jalalifar and Aziz (2012) were among the people who used finite element methods to model rock bolts in shear using the surface-to-surface contact model in Ansys. Nie et al. (2014) conducted an extensive numerical study on anchor bolts, D-bolts, split sets, and fully encapsulated bolts in pull out tests subject to multiple loading conditions such as drop testing using discontinues deformation analysis.

Mortazavi and Alavi (2013) used FLAC3D to model fully grouted rock bolts subjected to dynamic loading and investigated various termination configurations. Chen (2016) utilised FLAC2D to model pull out experiments done on plain Superstrand and bulbed MW9 cables in a modified LSEPT setup. The *rockbolt* element in FLAC was chosen as it can model the strain-softening behaviour seen in the tests (especially the MW9 cable). The result showed a very good correlation to the experimental data. Tahmasebinia et al. (2023) utilized Abaqus to model the double shear test on cable bolts in static loading following Tahmasebinia's et al. (2018, 2021) studies on dynamic response of cable bolts using the same numerical package, suggesting a cost-effective method to model cable bolts subjected to drop shear testing.

Numerical packages

According to Martin (2012), CESAR-LCPC is finite element software developed by the French LCPC (Laboratoire Central des Ponts et Chaussées) that provides a reinforcing element especially aimed at ground interactions. This one-dimensional element can only carry tensile or compressive loads. The model does not incorporate the grout as a separate medium due to its much lower stiffness compared to the cable. Instead, the grout, with an assumption of uniform shear distribution, is modelled through cable interface properties such as stiffness (E), tensile strength, cohesion, friction angle, dilation angle and interface shear stiffness (G_s) which can be acquired by laboratory testing in similar conditions to the field or, according to Al Hallak (1999), be a function of the cohesion and friction angle.

VIPLEF is a finite element numerical package capable of running general constitutive model codes developed at ParisTech (Martin, 2012). The package is capable of modelling fully grouted bolts. The bolts are modelled using two sets of 3 node elements which allows them to carry axial and bending loads by having the cross-sectional area, second moment, Young's modulus, and Poisson ratio of the

---

1 *Centre for Future Materials, University of Southern Queensland, Email: Rastegarmanesh@gmail.com*
2 *School of Civil Engineering and Surveying, University of Southern Queensland, Email: Ali.Mirzaghorbanali@unisq.edu.au*
3 *School of Civil Engineering and Surveying, University of Southern Queensland, Email: Kevin.McDougall@unisq.edu.au*
4 *School of Civil, Mining & Environmental Engineering, University of Wollongong, Email: Naj@uow.edu.au*
5 *School of Civil, Mining & Environmental Engineering, University of Wollongong, Email: sinaanzanpour@gmail.com*
6 *Centre for Future Materials, University of Southern Queensland, Email: Hadi.Nourizadeh@unisq.edu.au*

bolt. The interface of the bolt and the confining media is modelled using a high normal stiffness K_n and a stress-slip relationship developed by Jomaa (2003) in which the normal pressure acting on the interface is related to the slip using a series of parameters that can be attributed to grouting.

RS2 (formerly known as Phase2) is a finite element package cable for modelling cable bolts in civil and mining applications. The plain strand formulation of Phase 2 was based on Hyett et al. (1995), Moosavi et al. (1996), Hyett et al. (1996), and Moosavi (1997). The plain strand models consider the bolt as a single element and the stiffness of the grout, and the interfacial stiffness and strength of the bolt/grout interface is also included. The model only fails through the cable rupture as the bolt/grout interface is assumed to always be in a plastic state and the load transfer is based on the relative slip and the interface stiffness. Two types of modified geometry (25mm Garford bulb and 21mm nutcage) can be added to the model. A plain strand cable can be defined via borehole and cable diameters, cable elastic modulus, cable peak tensile load, W:C (to estimate the grout properties based on a database) and out of plain spacing.

Plaxis is another finite element package that can be used to model bolts. Although Plaxis does not explicitly offer a cable bolt option, the rock bolt function is strong and can be used in certain conditions. The pile model inherits its core from civil piles in the soil but can be assumed as a rock bolt embedded in rock or soil. The element is based on the Mindlin beam and is superimposed on the finite element mesh. The properties of the bolts and the interfacial behaviour are modelled with springs and sliders. The bolt/ground interaction is modelled by the skin and base resistance value in an elastoplastic model. When the shear resistance is reached, a permanent slip occurs.

FLAC and UDEC are finite-difference and discrete-element methods, respectively, that are popular in the mining and civil industry and can support bolts. In both pieces of software, the cable command refers to a one-dimensional element that can only undergo axial loading and cannot withstand bending. This element can model failure due to shear debonding. On the other hand, the rock bolt command denotes a two-dimensional element that can provide resistance to the lateral movement of the block (shearing of the discontinuity). Both forms of software consider the existence of the grout through its properties, not as a separate medium.

The cable is discretised onto smaller nodes with the mass of each segment at nodal points, and a spring/slider connection represents the bond. The model requires cable and hole diameters, cable elastic modulus, cable tensile load, grout compressive strength and shear modulus. For instance, FLAC was used by Ma et al. (2014) to model rock bolts, and the model input data was acquired using a push test on the bolts. The shear stress was assumed as the cohesion load over the surface area to which it was applied. The bolt failed at the joint surface where the maximum load was observed in the model.

All in all, a calibrated numerical model can help with understanding the role and effect of various parameters in the design of cable bolts. In the first sections of this study, a numerical approach is proposed and verified based on experimental data. Next, the calibrated model is tested to study various design elements through a series of sensitivity analyses.

NUMERICAL CONCEPT

A large scale pull out experiment consists of a cable encapsulated using either cementitious grout or resin in a concrete cylinder (Rastegarmanesh *et al.*, 2022, 2023; Anzanpour *et al.*, 2023). This cylinder is often encapsulated within a thick steel external confinement **Figure 1**. During the test, internal pressure inside the borehole increases as debonding and movement occurs. As damage starts to develop and dilation occurs, in many cases radial cracks emerge and propagate in the bonding agent annulus and the concrete confinement, reaching the metal external confinement.

This process can be a reasonable candidate for a Finite Element Method (FEM) approach. The software of choice for this study was Abaqus due to its extensive capability and robust explicit and implicit solvers. The experimental data used as a basis for this numerical study were gathered in a large-scale laboratory pull out test campaign by Rastegarmanesh et al. (2022) as seen in **Figure 1**.
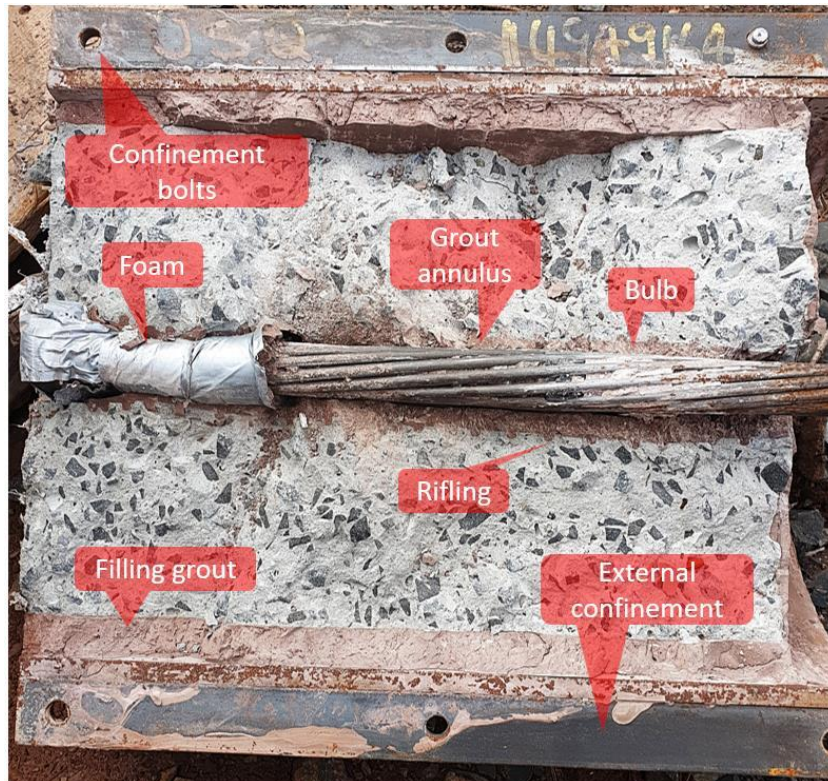
Figure 1: Different elements in a large scale laboratory pull out test on fully encapsulated cable bolts (Rastegarmanesh et al., 2022)

FINITE ELEMENT MODEL

A series of preliminary models were tested using Abaqus. While early full-size three-dimensional models showed potential, they clearly proved to be unnecessarily time-consuming and unstable to run. As a result, a number of simplifications were required in order to make the model computationally efficient. The next sections cover the proposed assumptions for the large-scale model.

Axisymmetry

Using engineering discretion to reduce a three-dimensional model into a two-dimensional numerical model reduces complexity and increases computational efficiency. Considering the cylindrical shape of the large-scale experiments, and interest in using the longitudinal cross-section of the samples to study the interfacial interaction of the cable and the annulus, the only viable option was Axisymmetry.

However, as cables are made by winding multiple strands together, they have out-of-plane rotations on them which makes axisymmetry invalid. Nevertheless, the advantages of a cost-effective two-dimensional model outweigh the added accuracy of the full three-dimensional model. Hence, each cable was modelled using revolution of the two-dimensional longitudinal section of the cable around the central axis.

Cables and External Confinement

Reducing the number of discretised sections in a finite element model can greatly improve efficiency. By examining experimental results and observations, it can be concluded that the damage in the model is created as a result of interaction of undamaged metal materials (i.e., cable and the external confinement – E>200 GPa) with the brittle materials (i.e., grout annulus, concrete confinement, and grout filling – E<50 GPa). Also, almost all damage and plastic deformations during the test happened in the breakable materials while the metal sections behaved well within their elastic limits.

As a result, the cable and external confinement in the model were assumed to be *rigid bodies* due to their negligible contribution compared to the grout and concrete. Modelling a cable as a single rigid body, instead of a deformable multi-strand discretised object with strands interacting with one another, significantly reduces the time of the runs and is a compromise worth making. Also, assuming a pinned

or roller boundary condition for the far end of the concrete block instead of a metal discretised object (i.e., outer confinement), further increases the efficiency.

The cables were all three-dimensionally modelled in AutoCAD using their geometrical properties (**Table 1**). A two-dimensional longitudinal section of the three-dimensional cable model was then taken (**Figure 2**). The two-dimensional representations of the cable had the shape of the outer strands of the cable. For the bulbed cables, a bulging section was added to the cable to represent the enlarged structure. Lastly, the indented cables were modelled using the properties of the interaction model as highlighted later on.

Table 1: Cable geometrical attributes (all dimensions in mm)

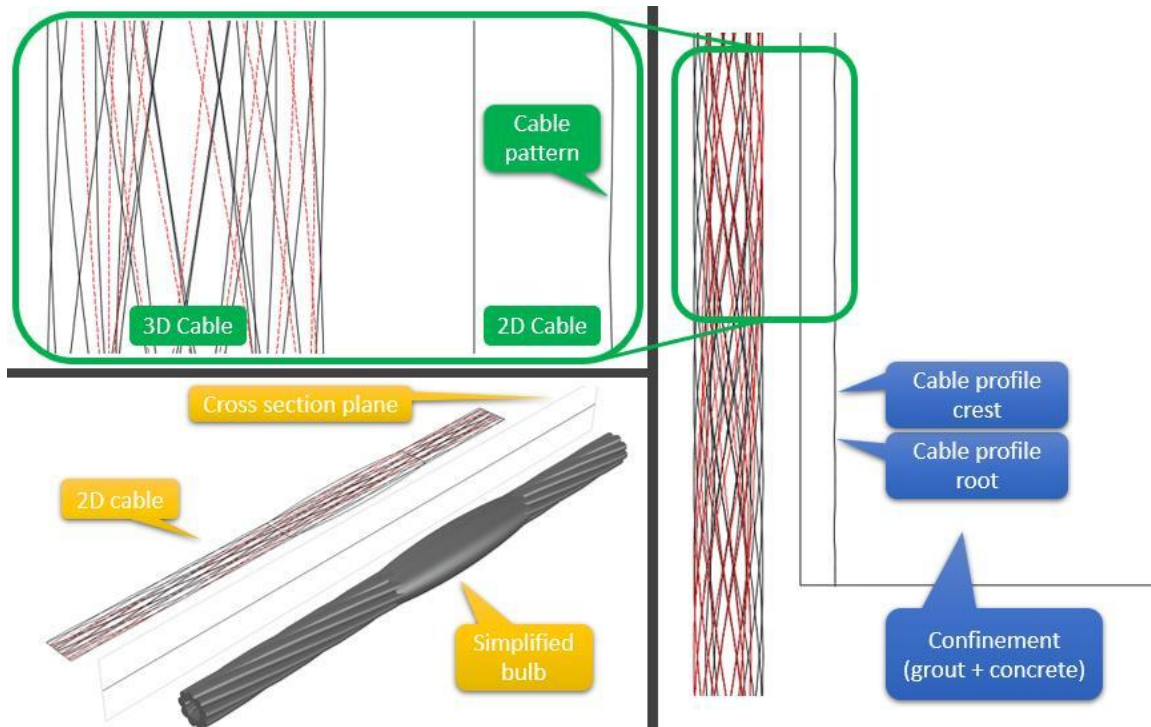| Cable	Total Diameter	Bulb Diameter	Strand Diameter	Number of Outside Strands	360° Rotation Length
SS, IDS	21.8	-	6	9	380
Gol	28.6	-	5 & 7	12	440
9S	28--35	7	7.5	9	470
10S	31--36	5	7	10	760
12S	31--36	5	6.5	12	520

Figure 2: Cable representation in a two-dimensional space

Constitutive Model

For grout and concrete, the Concrete Damage Plasticity (CDP) model, a well-defined and researched model for brittle materials such as concrete, grout and rock, was chosen. Both concrete and the grout are cementitious based materials that portray a brittle failure type. Consequently, the input variables for CDP can be extracted from the UCS tests as well as typical values for cementitious materials.

The CDP model includes the compressive and tensile behaviour of a material according to **Figure 3**. Damage parameters (d_t, d_c) are defined for both cases as a function of the strain, temperature (θ), or a pre-defined field variable (f_i), to degrade the uniaxial strengths (σ_t, σ_c). Damage values can range from 0 to 1 to represent undamaged to fully damaged material (equation 1).
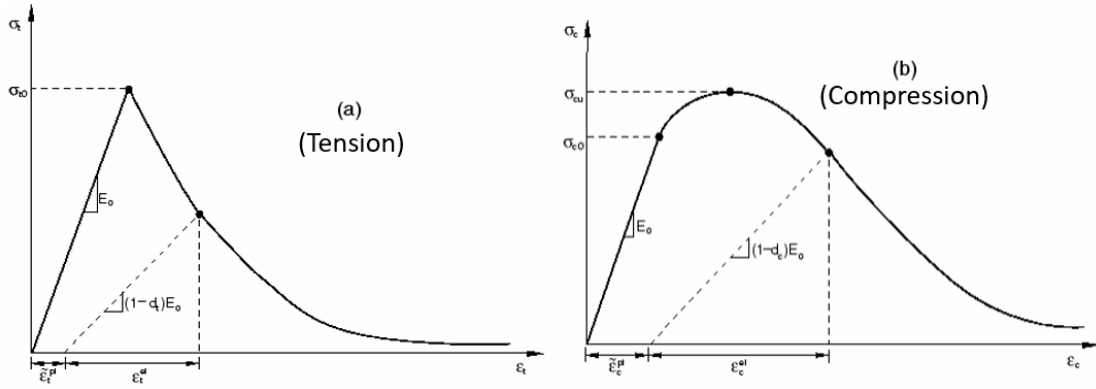
Figure 3: CDP model parameters (Abaqus, 2016)

In equation 1, d_t, d_c, σ_t, and σ_c represent damage and strength for tension and compression, respectively. Damage is a unitless value while strengths are reported in Pascal. $\tilde{\varepsilon}_t^{pl}$ and $\tilde{\varepsilon}_c^{pl}$ denote equivalent plastic strain and E_0 represents the initial (undamaged) elastic modulus. $\bar{\sigma}_t$ and $\bar{\sigma}_c$ refer to effective stresses which will be used to propose the yield surface in equation 2.

$$d_t = d_t\left(\tilde{\varepsilon}_t^{pl}, \theta, f_i\right), \quad \left(0 \le d_t \le 1\right) \tag{1}$$

$$d_c = d_c\left(\tilde{\varepsilon}_c^{pl}, \theta, f_i\right), \quad \left(0 \le d_c \le 1\right)$$

$$\sigma_t = \left(1 - d_t\right) E_0 \left(\varepsilon_t - \tilde{\varepsilon}_t^{pl}\right)$$

$$\sigma_c = \left(1 - d_c\right) E_0 \left(\varepsilon_c - \tilde{\varepsilon}_c^{pl}\right)$$

$$\bar{\sigma}_t = \frac{\sigma_t}{\left(1 - d_t\right)} = E_0 \left(\varepsilon_t - \tilde{\varepsilon}_t^{pl}\right)$$

$$\bar{\sigma}_c = \frac{\sigma_c}{\left(1 - d_c\right)} = E_0 \left(\varepsilon_c - \tilde{\varepsilon}_c^{pl}\right)$$

Figure 4 shows the yield surface for the CDP model based on equation 2 in which $\hat{\bar{\sigma}}_{max}$ is the maximum principal effective stress, $\sigma_{b0} / \sigma_{c0}$ is the ratio of initial equibiaxial compressive yield stress to initial compressive yield stress, K_c is the ratios of the second invariant on the tensile meridian (TM) to the compressive meridian (CM) at initial yield for any given value of the pressure invariants p, and $\bar{\sigma}_t\left(\bar{\varepsilon}_t^{pl}\right)$, $\bar{\sigma}_c\left(\bar{\varepsilon}_c^{pl}\right)$ are the effective tensile cohesion and compressive cohesion stresses.

$$F\left(\bar{\sigma}, \tilde{\varepsilon}^{pl}\right) = \frac{1}{1-\alpha}\left(\bar{q} - 3\alpha\bar{p} + \beta\left(\tilde{\varepsilon}^{pl}\right)\left\langle\hat{\bar{\sigma}}_{max}\right\rangle - \gamma\left\langle-\hat{\bar{\sigma}}_{max}\right\rangle\right) - \bar{\sigma}_c\left(\tilde{\varepsilon}_c^{pl}\right) \le 0 \tag{2}$$

$$\alpha = \frac{\left(\sigma_{b0} / \sigma_{c0}\right) - 1}{2\left(\sigma_{b0} / \sigma_{c0}\right) - 1}; 0 \le \alpha \le 0.5$$

$$\beta = \frac{\bar{\sigma}_c\left(\bar{\varepsilon}_c^{pl}\right)}{\bar{\sigma}_t\left(\bar{\varepsilon}_t^{pl}\right)}\left(1 - \alpha\right) - \left(1 + \alpha\right)$$

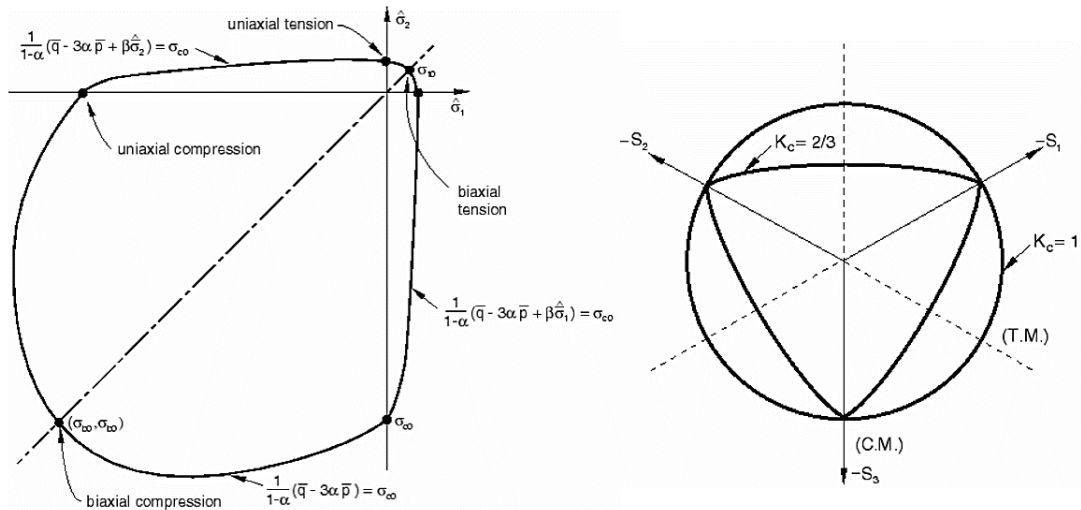$$\gamma = \frac{3\left(1 - K_c\right)}{2K_c - 1}$$

Figure 4: Yield surface in plane stress and deviatoric plane (Abaqus, 2016)

Table 2 and **Table 3** showcase the adopted values for the concrete and grout, based on their UCS tests. In both cases, the dilation angle, eccentricity, fb0/fc0, k, and viscosity parameters were assumed to be the default values (i.e., 35, 0.1, 1.16, 0.6667, and 0, respectively). Concrete and grout elastic properties were assumed to be according to Table 4 for simplicity, and later sensitivity analysis was conducted on these values.

Table 2: CDP inputs for the concrete confinement

Compression Hardening		Tension Stiffening		Compression Damage		Tension Damage	
Inelastic Strain	Yield Stress (Pa)	Inelastic Strain	Yield Stress (Pa)	Damage Parameters	Inelastic Strain	Damage Parameters	Inelastic Strain
0.00E+00	4.17E+07	0.00E+00	6.12E+06	0.00E+00	0.00E+00	0.00E+00	0.00E+00
1.09E-03	4.95E+07	2.26E-04	5.00E+06	4.00E-02	1.09E-03	1.80E-01	2.26E-04
2.65E-03	4.52E+07	6.24E-04	3.83E+06	8.00E-02	2.65E-03	3.80E-01	6.24E-04
4.38E-03	3.79E+07	8.21E-04	3.30E+06	2.30E-01	4.38E-03	4.60E-01	8.21E-04
6.07E-03	3.13E+07	1.02E-03	2.75E+06	3.70E-01	6.07E-03	5.50E-01	1.02E-03
7.71E-03	2.57E+07	1.57E-03	1.84E+06	4.80E-01	7.71E-03	7.00E-01	1.57E-03
9.28E-03	2.16E+07	1.94E-03	1.24E+06	5.60E-01	9.28E-03	8.10E-01	1.94E-03
1.04E-02	1.90E+07	8.76E-03	8.50E+05	6.20E-01	1.04E-02	8.60E-01	8.76E-03
1.39E-02	1.28E+07			7.40E-01	1.39E-02		
1.76E-02	8.50E+06			8.30E-01	1.76E-02		

Table 3: CDP inputs for the grout

Compression Hardening		Tension Stiffening		Compression Damage		Tension Damage	
Inelastic Strain	Yield Stress (Pa)	Inelastic Strain	Yield Stress (Pa)	Damage Parameters	Inelastic Strain	Damage Parameters	Inelastic Strain
0.00E+00	6.13E+07	0.00E+00	9.00E+06	0.00E+00	0.00E+00	0.00E+00	0.00E+00
1.60E-03	7.28E+07	3.32E-04	7.35E+06	4.00E-02	1.60E-03	1.80E-01	3.32E-04
3.90E-03	6.65E+07	9.18E-04	5.63E+06	8.00E-02	3.90E-03	3.80E-01	9.18E-04
6.44E-03	5.58E+07	1.21E-03	4.85E+06	2.30E-01	6.44E-03	4.60E-01	1.21E-03
8.93E-03	4.60E+07	1.50E-03	4.05E+06	3.70E-01	8.93E-03	5.50E-01	1.50E-03
1.13E-02	3.78E+07	2.31E-03	2.70E+06	4.80E-01	1.13E-02	7.00E-01	2.31E-03
1.36E-02	3.18E+07	2.86E-03	1.83E+06	5.60E-01	1.36E-02	8.10E-01	2.86E-03
1.53E-02	2.80E+07	1.29E-02	1.25E+06	6.20E-01	1.53E-02	8.60E-01	1.29E-02
2.05E-02	1.88E+07			7.40E-01	2.05E-02		
2.58E-02	1.25E+07			8.30E-01	2.58E-02		

Table 4: Initial assumed mechanical properties for concrete and grout

Type	Young's Modulus (GPa)	Poisson's Ratio	Density (kg/m^3)	Plasticity Model
Grout	50	0.25	2200	CDP
Concrete	50	0.2	2300	CDP

Finally, after testing various mesh sizes, the final model had a mesh size of 0.006 based on the performance of the axisymmetry model. This value, albeit not ideal, provided a balance point between the computation cost and accuracy. The element types for the cable and confinement were RAX2 (2-D linear axisymmetric rigid link) and C4X4R (4-node bilinear axisymmetric quadrilateral reduced integration), respectively.

Interaction Model

As rifling was used for the annulus/concrete interaction in the experimental tests, all slippage was attributed to the cable/annulus surface. The interaction between the cable and the grout annulus is the most important part of the model as it is the initiator of the load and damage transfer. Various interaction models were available, however, due to the complexity of the model and number of unknowns present, it was decided to use a simple *exponential decay* friction model.

Equation 3 outlines the general frictional model in Abaqus using the *exponential static-kinetic* frictional model. In the general friction model, the friction coefficient μ is a function of temperature ($\bar{\theta}$), field variable ($\bar{f}^\alpha$), equivalent slip rate ($\dot{\gamma}_{eq}$) and contact pressure (p). In the exponential static-kinetic frictional model, μ_s and μ_k are *static* and *kinetic friction coefficients* and d_c is the *decay coefficient* (**Figure 5**). The *decay coefficient* governs how fast μ_s morphs into μ_k (i.e., the progression from static to kinetic state which is an analogy to the transition from cohesional to frictional behaviour). The smaller the value, the faster the transition.

$$\mu = \mu\left(\dot{\gamma}_{eq}, p, \bar{\theta}, \bar{f}^\alpha\right) \tag{3}$$

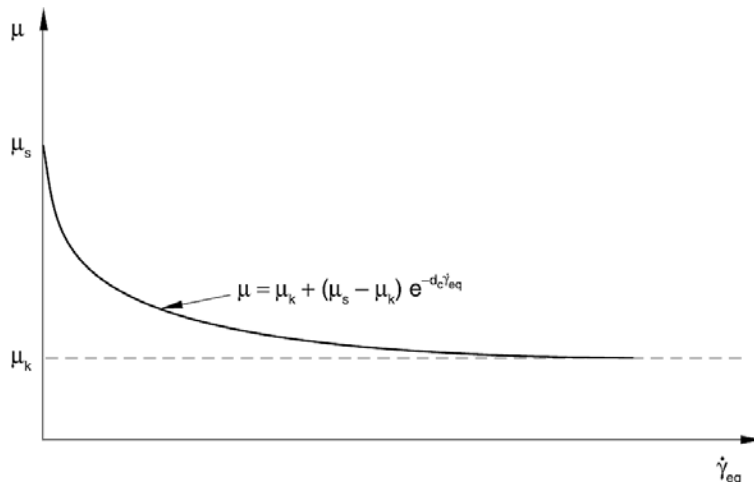$$\mu = \mu_k + \left(\mu_s - \mu_k\right)e^{-d_c\dot{\gamma}_{eq}}$$

Figure 5: Exponential decay friction model (Abaqus, 2016)

In this concept, in order to model the damage on the cable/grout interface, a high *static friction coefficient* is exponentially reduced to a *kinetic friction coefficient*. This way, the *static coefficient* can be a proxy for the *chemical bond strength* and the *kinetic coefficient* can be treated as an analogy to the *mobilised frictional strength* as the cable is pulled out. The process of finding and calibration of these two values as well as the *decay factor* was empirically based on the values available from the

experimental campaign. The input values for the model were as presented in Table 5 based on the following descriptions:

- For the plain cables (SS, IDS, and Gol), the difference between the μ_s and μ_k were 0.01, throughout. For the bulbed cables (9, 10, and 12S), the value was 0.03. The reasoning for this proposition was based on the evaluation of the condition of the grout ridges after the experimental testing in which the unbulbed cable had minimal damage while the bulbed cable had significant damage.
- Between the Superstrand and Goliath cable, it seemed for every millimetre diameter increase, the frictional values increased by 0.01.
- For the 9, 10, and 12S cables, differentiating based on diameter similar to the plain cables was not feasible since the bulbed cables are all almost identical in diameter. Also, the experimental findings have proved the presence of bulbs completely dominates the behaviour of the tests. Moreover, experimental results suggested all the bulbed cables act almost similarly. As a result, the bulbed cables were differentiated using the decay coefficient.
- Based on the observations from the large-scale experiments, a range was suggested based on the tendency of the cable to damage the grout annulus. In this model, Superstrand cable being a smooth, plain and the smallest cable had the proposed value of 0.7, and on the other side of the spectrum, 10 and 12 strand cables being the largest bulbed cables had the maximum decay value of 0.1. It is worth noting that the lower the decay coefficient, the faster the loss of initial undamaged resistance. In another words, larger unwieldier cables inflict more damage to the annulus earlier.
- The basis for the change in decay coefficient was in order: smoothness, indentation, bulb presence, and diameter.

Table 5: Interaction model inputs

Cable	Total Diameter	μ_s	μ_k	Decay Coefficient	Comment
Superstrand	21.8	0.02	0.01	0.7	
Indented Superstrand	21.8	0.1	0.09	0.5	Indentation caused higher μ_s and μ_k, and decreased the decay coefficient
Goliath	28.6	0.08	0.07	0.7	Increase in diameter compared to SS increased the μ_s and μ_k
9 Strand	35	0.04	0.01	0.3	Smaller diameter caused higher decay coefficient compared to 10S
10 Strand	36	0.04	0.01	0.1	Bulb presence decreased the decay coefficient compared to unbulbed cables
12 Strand	36	0.04	0.01	0.1	

Boundary conditions

At this point, the model consisted of two overall parts for *cable* and *confinement*. The *cable* was a rigid body that was governed by a single reference point. The reference point received a X direction symmetry boundary to prohibit movement along the X axis (Axis-1) as well as rotation around the Y and Z axes (Axis-2 and Axis-3). A quasi-static displacement of 100 mm along the Y axis was applied to the cable reference point (**Figure 6**).

The *confinement* section consisted of two parts for annulus and concrete. These two were in fact one part (due to rifling), but had different mechanical properties assigned to them based on the diameter of the borehole. Similar to the large-scale experiments, the upper surface of the concrete was constrained in the Y direction to inhibit vertical movement of the model. Moreover, the rightmost section of the concrete was constrained in the X direction to stop horizontal movement and react against the dilational force from inward. This boundary condition resembled the outer metal confinement of the experiments.
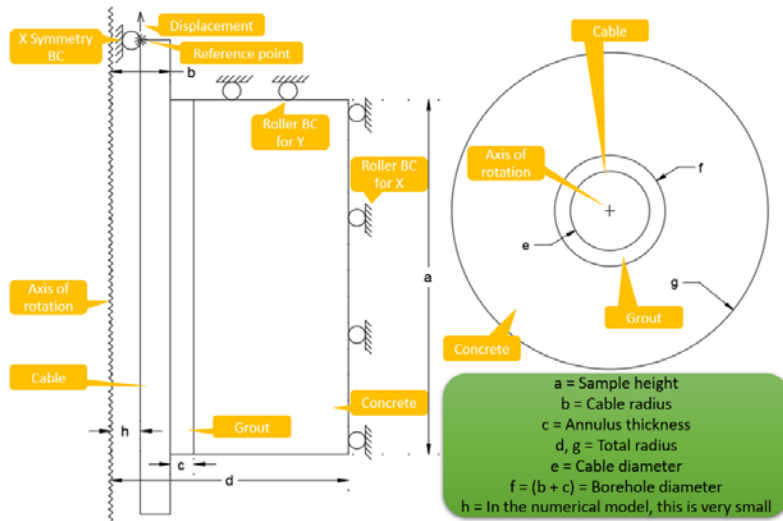
Figure 6: Boundary conditions and the model configuration for the models

NUMERICAL RESULTS

In total, data for 10 grout tests were used for the model verification. As evident for the unbulbed cables from **Figure 7**, **Figure 8** and **Figure 9**, almost a similar type of behaviour was witnessed for these cables. In all cases, while the initial stiffness was accurate, the peak load happened at almost twice the displacement of the experimental peak load. However, the accuracy of the peak load was reasonable.
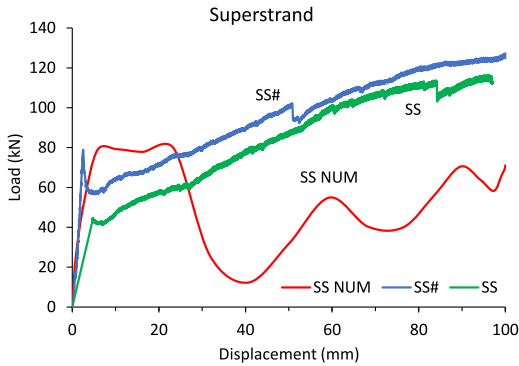

Figure 7: Numerical model results and comparison for Superstrand cable (# = rotation allowed)
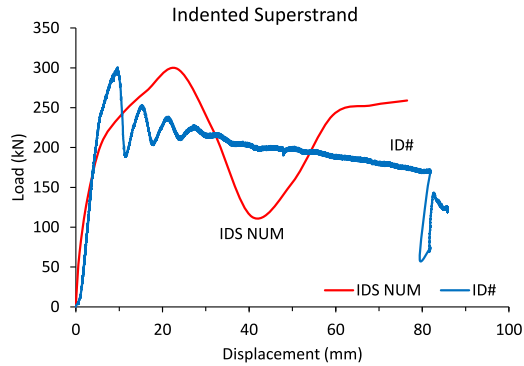
Figure 8: Numerical model results and comparison for indented Superstrand cable (# = rotation allowed
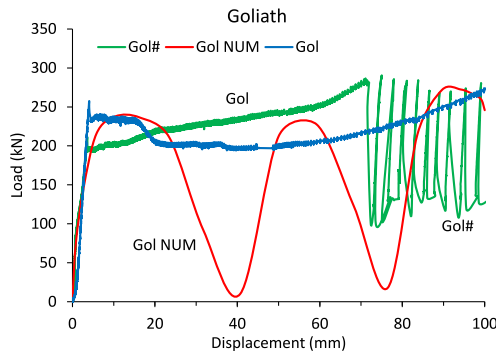
Figure 9: Numerical model results and comparison for Goliath cable (# = rotation allowed)

Furthermore, in all cases a unique post-peak behaviour was observed in which the load increased in cycles repeatedly. This behaviour resembles the post-peak oscillations in the bulbed cable. The spacing between these consecutive local extremums suggested probable relevance to the cables' longitudinal surface geometry which promotes jumping from one crest to another (**Figure 2**).

As the tests continue, the ridges suffer more damage, thus these distances decrease. As a result of assuming the cable to be a rigid two-dimensional body, the model in this study inherently models strands jumping between ridges during the pull-out instead of a rotational pull-out movement where the cable unscrews out of the grout annulus.

Figure 10, **Figure 11** and **Figure 12** illustrate completely different behaviour. For the bulbed cables, the model tended to be affected by the havoc caused by the bulbs, so a perfectly plastic to strain hardening behaviour was portrayed. The numerical model followed the oscillations' *peaks* for the full length of the pull-out with reasonable accuracy. Comparing the results to the unbulbed cables, this behaviour suggests no strand jumping (cable crests moving from root to root) was happening and the pull-out process was dominated by the mobilization and movement of the bulbs.
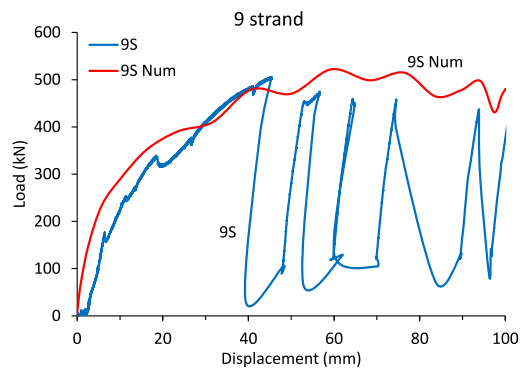
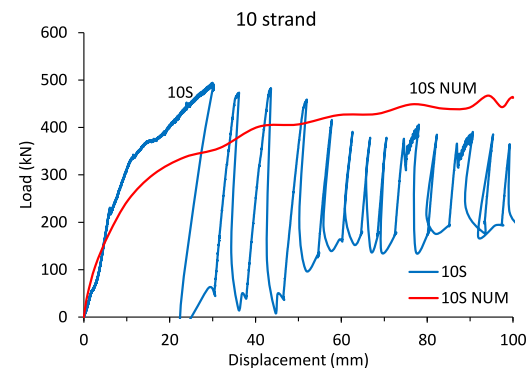**Figure 10: Numerical model results and comparison for 9 strand cable**

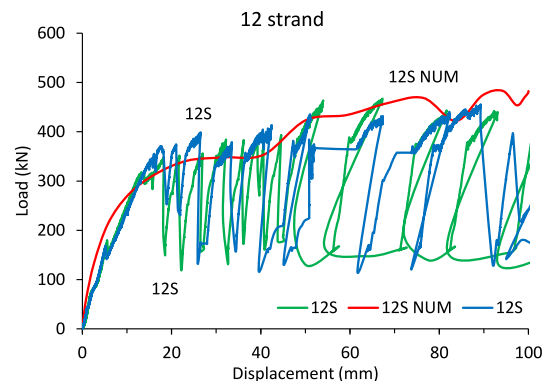**Figure 11: Numerical model results and comparison for 10 strand cable**

Figure 12: Numerical model results and comparison for 12 strand cable

Figure 13 and **Figure 14** present the stress distribution in the X direction (radial) for the 10 strand and Goliath cables during the course of the test, side by side. As seen, in the beginning, a compression zone (dark red) was formed above the bulb in the 10 strand cable. This compressive zone grows in size and magnitude as the test continues, creating deformed zones at the bottom and the top of the annulus. On the other hand, the unbulbed cable (Goliath) suggests compressive stress concentration and growth on the roots of the cable profile, where the grout is pushed by the cable crest.

These zones grow and merge together as the test progresses. This verifies the strand jumping and is evidenced by post-peak oscillations in the numerical graphs of the unbulbed cables, whereas the rather perfectly plastic behaviour of the bulbed cables is a manifestation of their stress distribution in these figures. The formation of the crater at the exit point can also be seen with a concentration of compressive stresses.

Figure 15 illustrates the extent and the type of the damage at the end of the test on the grout and the concrete based on the CDP model for 9 strand and Superstrand cables. The parameter D is between

0-1 and represents the degree of damage. As seen, the damage matches the distributions of the stress explained above. In the bulbed cable, a big compression damaged zone was formed above the bulb (including half the length of the bulb) with another zone at the entry point on the bottom. The same is true for the Superstrand cable as well, in which the failed elements in compression are mostly located at the cable cross sections' roots.
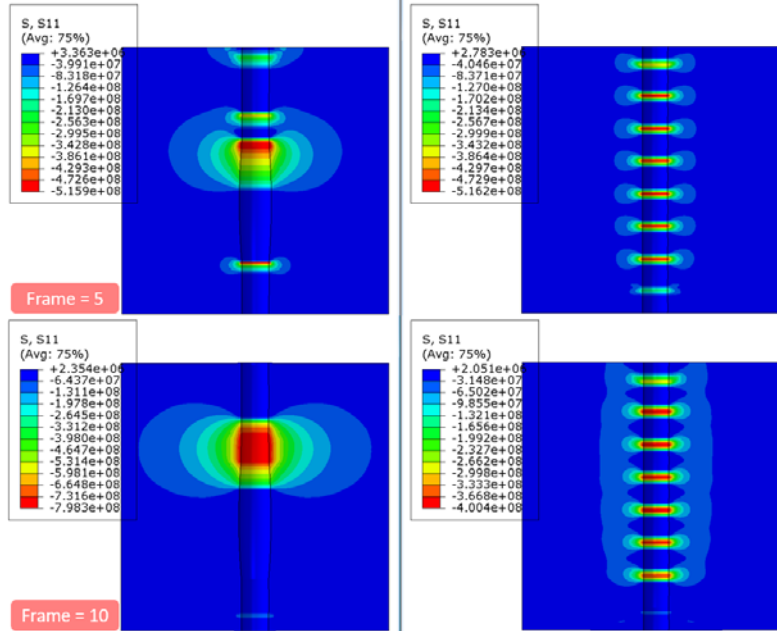

Figure 13: Stress development in X direction for the 10 strand (left) and Goliath (right) cable during the test - values in Pascal and compression is negative (frame 5 and 10 while frame 20 is the final frame)
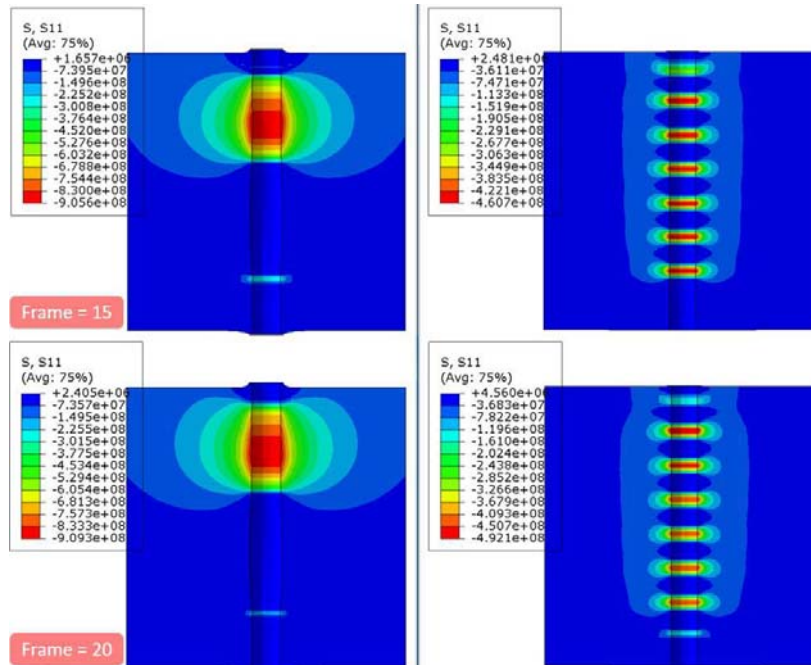
Figure 14: Stress development in X direction for the 10 strand (left) and Goliath (right) cable during the test - values in Pascal and compression is negative (frame 15 and 20 while frame 20 is the final frame)

As for the elements damaged in tension, the tensile damage is concentrated on the crests, suggesting as the elements in between the crest are squeezed (fail in compression), the elements at crests are extended (fail in tension). The same also holds valid for the bottom half of the bulb, where tensile

damage has developed. The most extensive tensile damage zone has formed at the entry point on the bottom where the failed elements have almost reached the outer boundary conditions of the model in the 9 strand case.

It should be noted that this phenomenon is incongruent with the experimental observations. The reason goes back to the innate limitation of the model as not being capable of simulating the unscrewing effect of the cable at the entry point, leading to false damage due to the entry point not having a boundary condition.

Nevertheless, it should be noted that while at a high enough load crack emergence is inevitable, compression damage typically results in broken or crushed material whereas tensile failure in brittle materials such as concrete leads to cracks. So, when a substantial tensile zone has formed anywhere in the model, it is typically safe to assume the model has developed radial cracks.
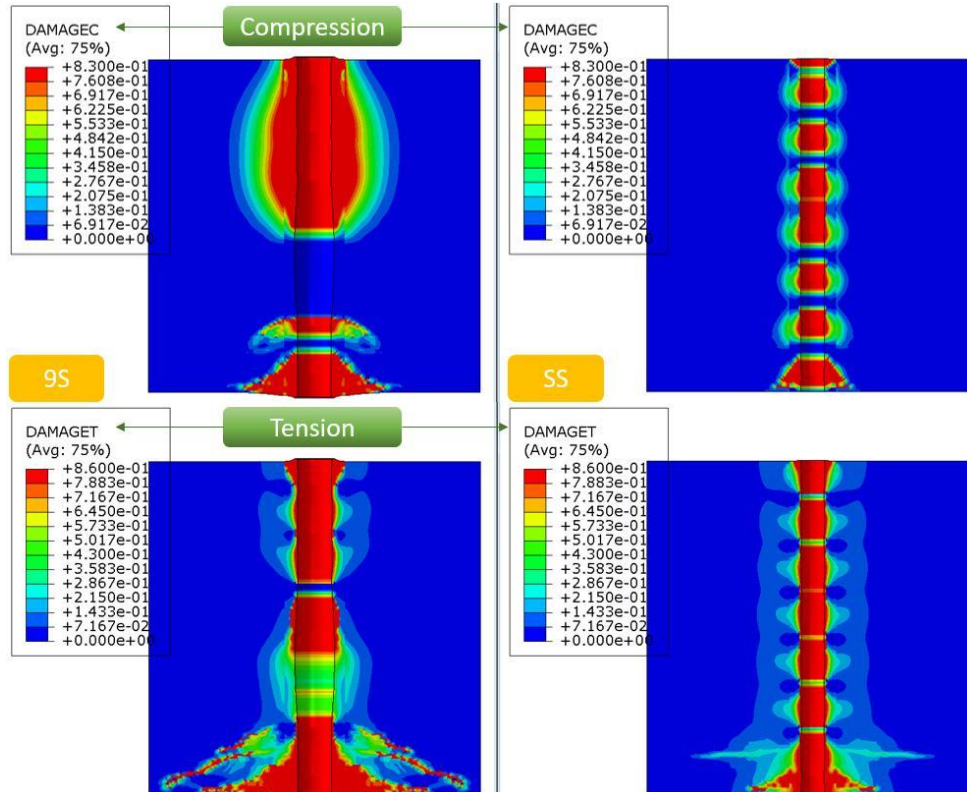
Figure 15: Tensile and compressive damage at the end of the tests for the 9 strand (left) and Superstrand cables (right) – pull direction is up

SENSITIVITY ANALYSIS

After model calibration and proposing the values and approaches that were successful in modelling the large-scale pull-out experiments, a series of sensitivity analyses were conducted to investigate the role of some of the important parameters in the design. In this section, sensitivity studies were conducted on Superstrand and 9 strand cable to be representative of plain and bulbed cables.

Figure 16 and **Figure 17** show the effect of the elastic modulus in the Superstrand and 9 strand cables. As the annulus and concrete cylinder comprise the total confinement, the value for E is changed simultaneously for both, to simulate the changes in the stiffness of the confinement during the test. As expected, an increase in elastic modulus increases the initial stiffness of both the Superstrand and 9 strand cables. This increase is maintained during the whole test. Similar observations were made in the experimental chapters by testing two values of torque on the confinement bolts.
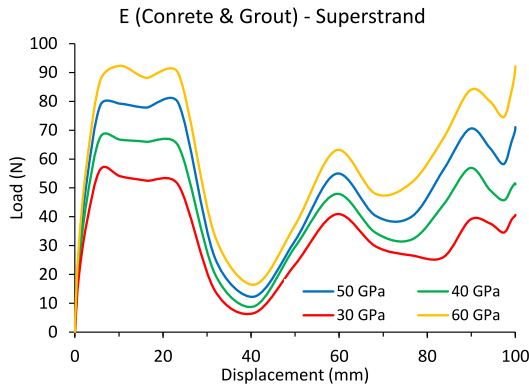
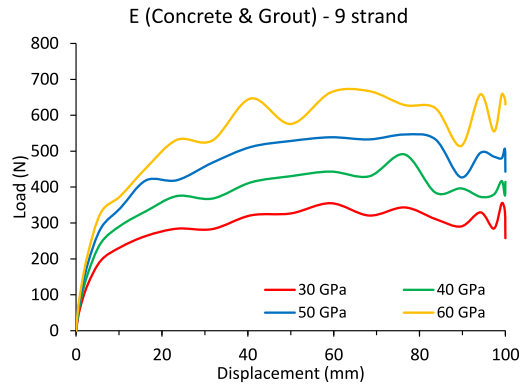**Figure 16: Effect of concrete and grout elasticity modulus for Superstrand cable**

Figure 17: Effect of concrete and grout elasticity modulus for 9 strand cable

Figure 18 and **Figure 19** illustrate the effect of the UCS of concrete for the Superstrand and 9 strand cables. Similar to the elastic modulus, an increase in UCS results in overall increase in the load-carrying capacity of the model for both cables. This increase tends to be the greatest when the UCS is increased from the low value of 20 MPa to 40 MPa, with 40MPa and 60 MPa being closer in performance. When the UCS is increased from 20 to 100 MPa, the Superstrand cable achieved around 30% higher load while the 9 strand cable has more than 100% load gain, suggesting more benefit for the bulbed cable.
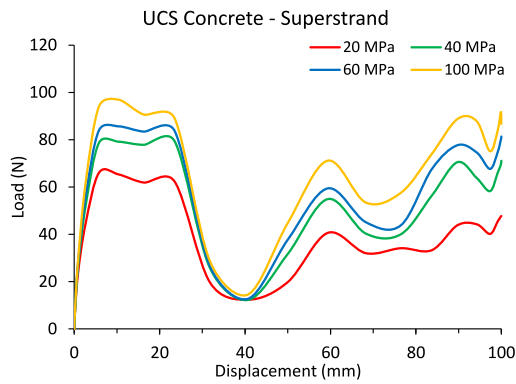

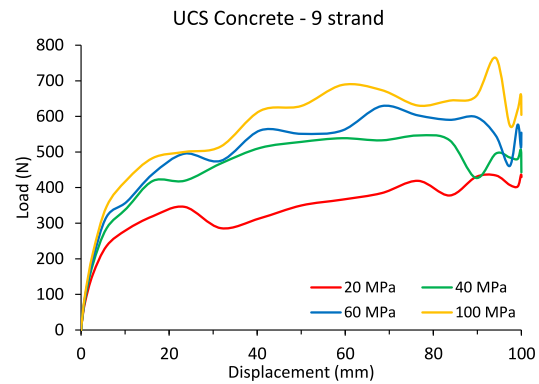**Figure 18: Effect of concrete UCS for Superstrand cable**

Figure 19: Effect of concrete UCS for 9 strand cable

Figure 20 and **Figure 21** illustrate the effect of the grout annulus UCS on the pull-out test. For the case of the Superstrand cable, the overall trend seems to be an almost identical effect to the concrete UCS value (**Figure 18**). However, after the first peak, the order of the UCS values is more irregular, suggesting more sensitivity to the grout strength in the post-peak for plain Superstrand cable. On the other hand, **Figure 20** clearly shows that the 9 strand cable is significantly less sensitive to the grout strength with all the values almost mirroring each other. This was also inferred from the experimental results in which bulb presence decreased sensitivity to some of the other factors.

Figure 22 and **Figure 23** exhibit the influence of cable diameter in the pull-out test. In both cases, the cable diameter is changed ±2mm at a time from their benchmark size indicated by 0 (i.e., 21.8mm for Superstrand and 28mm for the unbulbed section of 9 wire strand). It should be mentioned that for the 9 wire strand cable, an increase in diameter was applied simultaneously to both the unbulbed and bulbed sections of the cable, uniformly.

As seen, thicker cables have stiffer behaviour with higher loads at lower displacements. However, it seems the Superstrand cable load increases by around 70% when the diameter changes from -2mm to +6mm (8mm size difference), however, 9 strand cable has only around a 50% load gain. When increasing cable diameters, an increase in loads is axiomatic, due to an increase in the surface contact area. Here, the bulbed cable once again proves less sensitive to the geometrical changes compared to the plain cable.
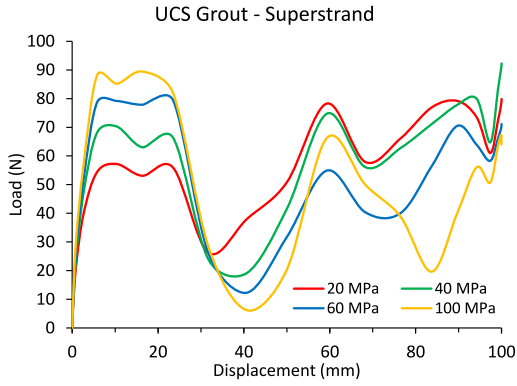
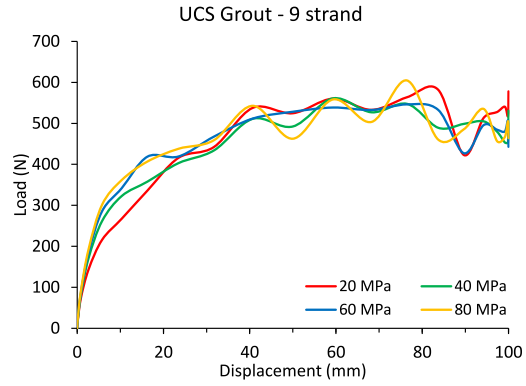**Figure 20: Effect of grout UCS for Superstrand cable**

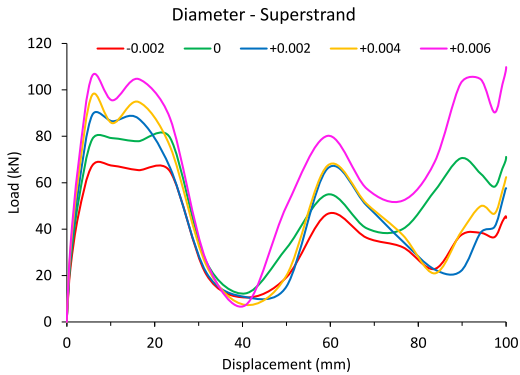**Figure 21: Effect of grout UCS for 9 strand cable**

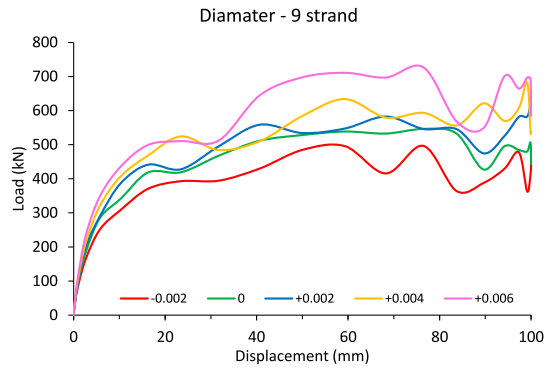**Figure 22: Effect of cable diameter for Superstrand cable**

Figure 23: Effect of cable diameter for Superstrand cable

Lastly, **Figure 24** shows how the bulb size alone can influence the results of the pull-out tests drastically. For this analysis, only the bulb diameter from the middle point (the thickest point) is changed while the unbulbed section of the 9 strand cable was unchanged. Changes in increments of ±2mm unequivocally illustrate the significant effect of bulb size in the model. In all cases, the loads increased by almost 100% as the bulb size is increased by just 2mm. A bulb size change of 6mm can increase the loading capacity of a system from less than 100kN to almost 900kN.
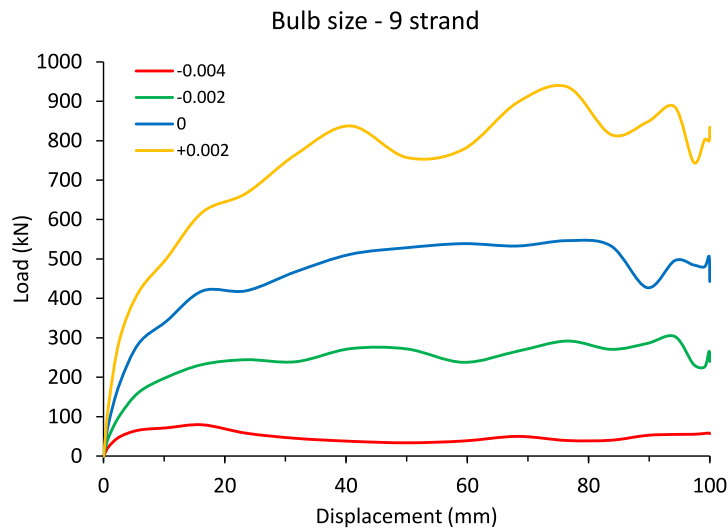

Figure 24: Effect of bulb diameter for Superstrand cable

SUMMARY

A reasonable accuracy was observed for the numerical models, especially for the bulbed cable. In the plain cables, the model failed to simulate the load attenuation in the post-peak zone and constantly overestimated the first peak displacement while predicting the overall load value highly accurately. In the bulbed cables, the model followed the peak loads of the oscillations closely, showing high potential. Furthermore, the damage output showed tensile and compressive damage zones were created due to stress concentrations around the cable crests and roots for the plain cable, and around the bulb, for the bulbed cable.

In the end, a series of sensitivity analyses were conducted on the calibrated models to study the effect of some of the parameters. It was seen that bulb size is the most influential parameter in the design. The cable diameter was a more important factor for the plain cable compared to the bulbed cable. Similarly, the bulbed cable showed less sensitivity to the grout strength compared to a plain cable while the concrete strength seemed to affect both to the same extent.

CONCLUSIONS

This study covered the numerical modelling approach using finite element (Abaqus) for the large-scale pull-out tests in grout. As a result, a two-dimensional axisymmetry model was preferred over a full-size three-dimensional model. This meant the out of the plain geometrical rotation of the cable was not taken into consideration. The cables were assumed to be rigid bodies to save computational cost. The grout and concrete were modelled using the Concrete Damage Plasticity model. Based on UCS testing of materials. Lastly, the interaction model for the cable/grout interface was assumed and calibrated to be a static-kinetic exponential decay model.

The plain cables in the numerical model all experienced load drops at almost twice the initial peak displacement, while the initial peak load value was simulated very accurately. Furthermore, the graphs failed to attenuate over time and kept oscillating. This suggested the numerical model lacked a more substantial mechanism to dissipate the loads over the displacement, though a plastic model was used.

The numerical model of the bulbed cables had the tendency to match the high bounds of the oscillations seen in the laboratory results. The lack of individual wires in the strand and the unscrewing effect in the numerical model led to the results being much smoother. The damage analysis after the numerical tests indicated that numerous compression and tension zones were developed for the plain cable at the crest/root interaction zones. However, for the bulbed cable, the damage was mainly attributed to the bulb movement, similar to the observations from the lab experiments.

Sensitivity analysis of the numerical models for elastic modulus and the UCS of concrete suggested that higher annulus strength was less important for a bulbed cable than a plain cable. Both the plain Superstrand and bulbed 9 wire strand cables showed high sensitivity to the diameter of the cable. The most significant changes, however, were witnessed in bulb size study in which a small 2mm change in bulb size caused 100% change in the load value.

As seen in the finite element method, even with the oversimplification of assumptions, the model can successfully be used for modelling the interaction and damage for the cable bolt axial behaviour. It is recommended to study the effect of the simplifications in this study such as axisymmetry and the interaction model and discover the optimal trade-off between the computational cost and accuracy. Moreover, other numerical techniques, in particular, Extended Finite Element Method (XFEM) can be of interest to study the crack initiation and propagation due to the cable mobilization in a pull-out test and later axial performance of cable bolts in the field.

ACKNOWLEDGEMENT

REFERENCES

Anzanpour, S., Aziz, N., Remennikov, A., Nemcik, J., Mirzaghorbanali, A. and Rastegarmanesh, A., 2023, Laboratory study of the behaviour of grouted cable bolts under static and dynamic axial

loading, *IOP Conference Series: Earth and Environmental Science*, 1124, p. 12095. Available at: https://doi.org/10.1088/1755-1315/1124/1/012095.

Chen, J., 2016, *Load Transfer Mechanism of Fully Grouted Cable Bolts*. University of New South Wales.

Al Hallak, R., 1999, *Etude expérimentale et numérique du renforcement du front de taille par boulonnage dans les tunnels en terrains meubles*. Marne-la-vallée, ENPC.

Hyett, A.J., Bawden, W.F., Macsporran, G.R. and Moosavi, M., 1995, A Constitutive Law for Bond Failure of Fully-grouted Cable Bolts Using a Modified Hoek Cell, *International Journal of Rock Mechanics and Mining Sciences & Geomechanics Abstracts*, 32(1), pp. 11–36.

Hyett, A.J., Moosavi, M. and Bawden, W.F., 1996, Load distribution along fully grouted bolts, with emphasis on cable bolt reinforcement, *International journal for numerical and analytical methods in geomechanics*, 20(7), pp. 517–544.

Jalalifar, H. and Aziz, N., 2012, *Numerical simulation of fully grouted rock bolts*. Wollongong. Available at: https://doi.org/10.5772/48287.

Jomaa, M., 2003, *Modélisation par éléments finis du soutènement par boulonnage*. ParisTech.

Ma, S., Nemcik, J. and Aziz, N., 2014, Simulation of fully grouted rockbolts in underground roadways using FLAC2D, *Canadian Geotechnical Journal*, 51, pp. 911–920.

Martin, L.B., 2012, *Theoretical and experimental study of fully grouted rockbolts and cablebolts under axial loads*. ParisTech.

Moosavi, M., 1997, *Load distribution along fully grouted cable bolts based on constitutive models obtained from modified Hoek cells*. Queen's.

Moosavi, M., Bawden, W.F. and Hyett, A.J., 1996, A comprehensive laboratory test program to study the behavior of modified geometry cable bolt support, in *Rock mechanics tools and techniques*, pp. 209–216.

Mortazavi, A. and Tabatabaei Alavi, F., 2013, A numerical study of the behavior of fully grouted rockbolts under dynamic loading, *Soil Dynamics and Earthquake Engineering*, 54, pp. 66–72. Available at: https://doi.org/10.1016/J.SOILDYN.2013.08.003.

Nie, W., Zhao, Z.Y., Ning, Y.J. and Sun, J.P., 2014, Development of Rock Bolt Elements in Two-Dimensional Discontinuous Deformation Analysis, *Rock Mechanics and Rock Engineering*, 47(6), pp. 2157–2170. Available at: https://doi.org/10.1007/S00603-013-0525-1/METRICS.

Rastegarmanesh, A., Mirzaghorbanali, A., McDougall, K., Aziz, N., Anzanpour, S., Nourizadeh, H. and Moosavi, M., 2022, Axial Performance of Cementitious Grouted Cable Bolts Under Rotation Constraint Scenarios, *Rock Mechanics and Rock Engineering*, 55(9), pp. 5773–5788. Available at: https://doi.org/10.1007/s00603-022-02950-4.

Rastegarmanesh, A., Mirzaghorbanali, A., McDougall, K., Aziz, N., Anzanpour, S., Nourizadeh, H. and Moosavi, M., 2023, Axial response of resin-encapsulated cable bolts in monotonic and cyclic loading, *Canadian Geotechnical Journal* [Preprint]. Available at: https://doi.org/10.1139/cgj-2022-0379.

Tahmasebinia, F., Yang, A., Feghali, P. and Skrzypkowski, K., 2023, Structural Evaluation of Cable Bolts under Static Loading, *Applied Sciences*, 13(3), p. 1326. Available at: https://doi.org/10.3390/APP13031326.

Tahmasebinia, F., Zhang, C., Canbulat, I., Vardar, O. and Saydam, S., 2018, Numerical and analytical simulation of the structural behaviour of fully grouted cable bolts under impulsive loading', *International Journal of Mining Science and Technology*, 28(5), pp. 807–811. Available at: https://doi.org/10.1016/J.IJMST.2018.08.012.

Tahmasebinia, F., Zhang, C., Wei, C., Canbulat, I., Saydam, S. and Sepasgozar, S., 2021, A new concept to design combined support under dynamic loading using numerical modelling, *Tunnelling and Underground Space Technology*, 117, p. 104132. Available at: https://doi.org/10.1016/J.TUST.2021.104132.